

Finite Element Comparison of Homogenous Ridged and Non-Ridged X-Band Rectangular Waveguide Structures

Samuel J. Wyss[†]

[†]School of Nuclear Engineering
Purdue University
West Lafayette, Indiana 47907
E-mail: wysss@purdue.edu

Abstract—Two dimensional Finite Element Analysis (FEA) is applied to assess dispersion characteristics of homogenous rectangular, circular and ridged X-Band waveguide structures. To model these systems *in silico*, the weak form of the wave equation is derived from Maxwell's Equations for both TE and TM modes. Perfect electrical conductors (PECs) are used as waveguide walls as to neglect the effect of wave leakage into the environment. The model is validated against the analytical dispersion curves for rectangular and circular waveguides. A comparison of dispersion characteristics for ridged and non-ridged rectangular waveguides is provided which is then used to assess real world applications of ridged waveguides.

I. INTRODUCTION

Waveguides are used in a plethora of applications ranging from transmitting microwave fields to acting as passive low-pass filters [1]. While any cross section of a single conductor waveguide can support TE and TM modes, rectangular and circular cross sections are commonly chosen due to their ease of construction and analytic propagation characteristics. However, a limitation of rectangular waveguides is the limited bandwidth of their dominant mode which is less than an octave [1]. By adding a single or double ridge to the mouth of a waveguide, the cutoff frequency of the dominant mode can be reduced thus allowing for increased signal bandwidth [1]. This increased bandwidth comes at the cost of reduced power capacity due to the reduction in breakdown potential between the ridges [1] making them less ideal for High Power Microwave (HPM) devices.

Finite element description, applicability of FEM

Description of paper with explicit section references

Rectangular cavity resonators are used in a variety of applications ranging from filters to microwave energy storage devices [1]. Furthermore, rectangular cavity resonators are popular due to their simplistic design which can easily be constructed by placing shorting planes on the wave ports, thereby limiting energy loss to dielectric and wall surface conductivity [1]. This simplistic design allows for precise control of the unloaded quality factor (Q) and resonance frequency of these resonators by simply changing material properties and cavity length for example.

All wave phenomenon in waveguides and cavity resonators for a given frequency are derivable analytically from

Maxwell's Equations. Maxwell's Equations, namely Faraday's and Ampère's laws, can describe nearly all wave interactions in electromagnetics to a level of precision that few areas in physics can match [2]. In 1966, Kane S. Yee proposed a temporally and spatially staggered grid which could be used to explicitly solve Maxwell's Equations using finite differences in the time domain [3]. The staggered Yee grid positions the electric and magnetic fields on the edges of spatially offset voxels at half integer time-steps [3]. This method resolved many of the erroneous solutions from previous finite-difference solutions as it constructs fields able to be integrated over a line [2] much like the integral form of Maxwell's Equations.

Finite Difference Time Domain (FDTD) is well suited to model structures as TE_{10} waveguides and TE_{101} cavity resonators due to the similarity between device length and wavelength. This length symmetry allows for relatively few spatial and temporal 'points' to be used to obtain a full-wave solution in these geometries. In addition to this, FDTD facilitates the modeling of wide-band pulses allowing for results from large patches of the frequency domain to be obtained from a single simulation which is ideal for studying device resonances.

II. MATHEMATICAL MODEL

To model these systems *in silico*, the simulation domain must be divided up into regions where specific mathematical relations hold. For the purposes of this study, there are three such regions (i) PEC surrounded dielectric, (ii) Total Field / Scattered Field (TF/SF) 1-way source, and (iii) Mur's Absorbing Boundary Condition (ABC), all shown in Fig. 1. Regions (ii-iii) are essential for validation of the model as they will give the illusion that the waveguide is infinite in length allowing for propagation characteristics to be studied. To model a TE_{101} cavity resonator, Mur's ABC will be removed as to allow waves to resonate off of the PEC walls. The governing relations in each of these regions will be formulated and discretized to produce time-stepping formulas which allow the system to evolve transiently.

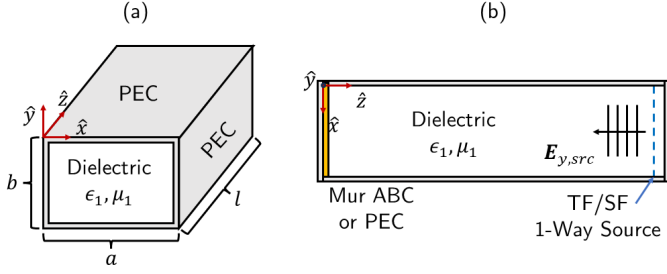


Fig. 1: Diagrams of (a) High-Level PEC Rectangular Waveguide (b) \hat{y} -Sliced Waveguide/Resonator Model with Labeled Regions

A. Model Formulation

1) *PEC Surrounded Dielectric*: As outlined in Fig. 1(b) the vast majority of the simulation domain is composed of a PEC enclosed dielectric, the governing equations of which are Ampère's and Faraday's Laws respectively. In differential form, these equations take the form

$$\nabla \times \mathbf{H} = \frac{\partial \mathbf{D}}{\partial t} + \mathbf{J} \quad (1)$$

and

$$\nabla \times \mathbf{E} = -\frac{\partial \mathbf{B}}{\partial t} - \mathbf{M} \quad (2)$$

where \mathbf{E} is the electric field, \mathbf{D} is the electric flux density, \mathbf{H} is the magnetic field, \mathbf{B} is the magnetic flux density, \mathbf{J} is the free electric current density, and \mathbf{M} is the fictitious free magnetic current density.

For simplicity, this analysis focuses on diagonally-isotropic, time-invariant, and non-dispersive dielectrics within the waveguide. Under these stipulations, each set of fields and flux densities, (\mathbf{E}, \mathbf{D}) , (\mathbf{H}, \mathbf{B}) , can be related using the following constitutive relations

$$\mathbf{D} = \epsilon \mathbf{E}, \mathbf{B} = \mu \mathbf{H} \quad (3)$$

with ϵ and μ as the permittivity and permeability of the dielectric respectively.

In this analysis, no fictitious magnetic conductors will be considered as they are not pertinent, thus $\mathbf{M} = 0$. The free electric current density is treated as a linear superposition of Ohmic conduction $\mathbf{J}_{Ohm} = \sigma \mathbf{E}$ and a source term \mathbf{J}_{src}

$$\mathbf{J} = \sigma \mathbf{E} + \mathbf{J}_{src} \quad (4)$$

where σ is the diagonally-isotropic, time-invariant dielectric conductivity.

In the described system, the inclusion of a source current density is not necessary as the wave is assumed to already be propagating in the waveguide from the TF/SF source. Despite this, this source current density will be included in the governing set of equations for completeness. The full set of governing equations for waves propagating within the dielectric are as follows:

$$\nabla \times \mathbf{H} = \epsilon \frac{\partial \mathbf{E}}{\partial t} + \sigma \mathbf{E} + \mathbf{J}_{src} \quad (5)$$

$$\nabla \times \mathbf{E} = -\mu \frac{\partial \mathbf{H}}{\partial t}. \quad (6)$$

Each of these 3D vector equations can be broken down into \hat{x} , \hat{y} , and \hat{z} component equations. Equations governing the \hat{y} components of \mathbf{E} and \mathbf{H} in (5-6) are

$$\frac{\partial H_x}{\partial z} - \frac{\partial H_z}{\partial x} = \epsilon \frac{\partial E_y}{\partial t} + \sigma E_y + J_{y,src}, \quad (7)$$

and

$$\frac{\partial E_x}{\partial z} - \frac{\partial E_z}{\partial x} = -\mu \frac{\partial H_y}{\partial t} \quad (8)$$

respectively.

These scalar equations are valid for all locations within the dielectric region excluding those inside of the PEC at which there is a Dirichlet boundary condition

$$E_x = E_y = 0. \quad (9)$$

This Dirichlet boundary condition originates from the conservation of tangential electric fields at medium boundaries

$$\hat{n} \times \mathbf{E}_1 = \hat{n} \times \mathbf{E}_2. \quad (10)$$

By nature of their infinite conductivity, electric fields cannot exist within in the PEC walls thus (10) gives rise to (9).

2) *TF/SF 1-way Source*: One of the most popular methods for injecting source fields into a simulation domain is via a TF/SF 1-way source [4]. The total-field, scattered-field formulation arises from the linearity of Maxwell's equations. Fields within the total-field region are a superposition of source fields and scattered fields. On the other hand, fields in the scattered field only consist of those reflected off of materials within the simulation.

As shown in Fig. 1, The TF/SF source is introduced in a plane with a normal vector $\hat{n} = -\hat{z}$. As outlined in [4], fields may be introduced on such planes by fully specifying E_x, E_y, H_x and H_y . For this analysis, the waveguide source fields will be restricted to E_y, H_x and H_z as in [5]. Thus for source fields originating on a \hat{z} plane, only the former two fields need to be specified.

To respect the Dirichlet boundary condition on PEC walls as defined in (9-10), the spatial distribution of the steady state frequency solution must be satisfied as to ensure all numerical results are physical. These time independent solutions are as follows

$$E_y = E_0 \sin \frac{\pi x}{a} \quad (11)$$

and

$$H_x = -\left(\eta \left[1 - \left(\frac{\omega_c}{\omega}\right)^2\right]^{-1/2}\right)^{-1} \left(E_0 \sin \frac{\pi x}{a}\right) \quad (12)$$

where E_0 is the initial complex valued waveguide intensity, a is the width of the waveguide as in 1, η is the intrinsic impedance of the waveguide dielectric, ω_c is the cutoff angular frequency of the waveguide, and ω is the angular frequency of the source field [5].

Converting (11-12) to the time-domain, the 1-way TF/SF

source formulation becomes

$$E_y = E_{y,src}(t) \sin \frac{\pi x}{a} + E_{scat} \quad (13)$$

and

$$H_x = -E_{y,src}(t) \left(\eta \left[1 - \left(\frac{\omega_c}{\omega} \right)^2 \right]^{-1/2} \right)^{-1} \left(\sin \frac{\pi x}{a} \right) + H_{scat} \quad (14)$$

in the total field region with E_{scat} as the scattered electric field, H_{scat} as the scattered magnetic field, and $E_{y,src}$ as a time-varying E_y source field.

The time-varying electric source field is specific to the desired simulation outcome. To obtain a response at a nearly monochromatic frequency, a tapered sine wave may be used, such as

$$E_{y,src} = E_0 \left[1 - \exp \frac{(t - t_d)}{\tau} \right] \sin \omega_0 t \quad (15)$$

where t_d is a delay time and τ is the temporal width of the ramping period. The tapered sine source gradually ramps-up to full field intensity reducing numerical artifacts from sudden jumps [2].

To obtain a wide-band simulation response, a modulated Gaussian pulse is ideal as it allows for the specification of frequency content via the temporal ramping period width τ and a carrier center angular frequency ω_0 [2], represented as

$$E_{y,src} = E_0 \exp \left(-\frac{1}{2} \left(\frac{t - t_d}{\tau} \right)^2 \right) \sin \omega_0 t. \quad (16)$$

3) *Mur's Absorbing Boundary Condition*: Mur's absorbing boundary condition is a discretized form of the 1-way Engquist-Majda wave equation [2], [4]. A three-dimensional, elliptic wave equation describing the evolution of an arbitrary scalar field U is given by

$$\frac{\partial^2 U}{\partial x^2} + \frac{\partial^2 U}{\partial y^2} + \frac{\partial^2 U}{\partial z^2} - \frac{1}{c} \frac{\partial^2 U}{\partial t^2} = 0 \quad (17)$$

as defined in [4].

Via algebraic manipulation, and a second order accurate, Taylor series expansion of the general expression $\sqrt{1 - s^2} \approx 1 - s^2/2$, the following continuous Engquist-Majda absorbing boundary condition at the $z = 0$ plane can be derived from (17) as

$$\frac{\partial^2 U}{\partial z \partial t} - \frac{1}{c} \frac{\partial^2 U}{\partial t^2} + \frac{c}{2} \frac{\partial^2 U}{\partial x^2} + \frac{c}{2} \frac{\partial^2 U}{\partial y^2} = 0 \quad (18)$$

as in [4].

To absorb the incident wave introduced in II-A2, (18) is used to absorb both E_y and H_x fields along the $z = 0$ which are introduced by the TF/SF 1-way source outlined in II-A2 at the opposite end of the simulation domain.

B. Discretization

To map the continuous equations above into data and structures that can be trivially represented using finite sequences of finitely precise numbers as found in all digital computer

systems, space and time need to be broken up into discrete steps.

Despite the implementation benefits of abstractly defining spatial and temporal steps as rational multiples of the wavelength and/or Courant number [6], it is far more useful from an engineering perspective to define concrete spatial and temporal steps. In the case of 3-dimensional waveguides, propagation is largely dependent on the exact sizes of the waveguide. Thus taking dynamic approach by first calculating a maximum spatial or temporal step needed to achieve a desired resolution and then snapping that to a desired value is chosen. For an arbitrary maximum spatial/temporal step Δs_{max} , a snapped Δs can be obtained using

$$\Delta s = \frac{s}{\lceil s/\Delta s_{max} \rceil} \quad (19)$$

where s is the 'length' of a spatial / temporal step [7]. This method ensures that any calculated Δs is always less than or equal to that of the precalculated maximum based on a set precision requirement. This method does come at the cost of adding additional temporal and points into the simulation domain which scales with $O(1)$ and $O(n^2)$ respectively for a 3-dimensional simulation.

In the case of spatial steps, the precalculated maximum step is the minimum of the set of steps required to resolve the minimum wavelength Δs_λ and the minimum feature size Δs_f each to a specified resolution as

$$\Delta s_{max} = \min(\Delta s_\lambda, \Delta s_f). \quad (20)$$

With the calculated values of Δx , Δy and Δz from (19)-(20) the maximal temporal discretization is obtained from the Courant-Friedrichs-Lewy stability condition [8], which states

$$\Delta t_{max} \leq \frac{1}{c \sqrt{\frac{1}{\Delta x^2} + \frac{1}{\Delta y^2} + \frac{1}{\Delta z^2}}} \quad (21)$$

where c is the wave velocity.

This calculated maximal temporal discretization is now able to be snapped to a concrete end time using (19) just as spatial steps were snapped to concrete distances.

For convenience, the following shorthand notation for discrete functions is introduced

$$f(x, y, z, t) \rightarrow f(i\Delta x, j\Delta y, k\Delta z, n\Delta t) \rightarrow f^n(i, j, k) \quad (22)$$

With space and time discretized into steps, it is now possible to define spatial and temporal grids for the governing equations in Section II-A to act on. As is the standard with finite difference methods in computational electromagnetics, the Yee Grid will be used to construct update equations [4]. Electric fields will be defined on the primordial grid with integer spatial and temporal indices whereas the magnetic field will be defined on the secondary grid which is offset by half spatial and temporal steps.

On this grid using the discrete shorthand outlined in (22) central spatial and temporal first-order derivatives can be expressed as

$$\frac{\partial f^n(i)}{\partial x} \approx \frac{f^n(i + \frac{1}{2}) - f^n(i - \frac{1}{2})}{\Delta x} \quad (23)$$

and

$$\frac{\partial f^n(i)}{\partial t} \approx \frac{f^{n+1/2}(i) - f^{n-1/2}(i)}{\Delta t} \quad (24)$$

respectively. Similar discrete forms of higher order derivatives are obtained taking the discrete derivative of discrete derivatives.

C. Time Stepping Equations

Time stepping update equations are now obtained by substituting discrete derivatives into the governing equations in Section II-A evaluated on the Yee grid. All magnetic field quantities are first evaluated at half integer time-steps which are then used to update electric fields at integer time-steps in a leap-frog fashion. If a field value is needed at a time or spatial index that does not exist, a spatial or temporal average is used.

1) *PEC Surrounded Dielectric*: Starting with the dielectric bordered PEC region, (7-8) can now be written as

$$\begin{aligned} & \frac{H_x^{n+1/2}(i, j + \frac{1}{2}, k + \frac{1}{2}) - H_x^{n+1/2}(i, j + \frac{1}{2}, k - \frac{1}{2})}{\Delta z} \\ & - \frac{H_z^{n+1/2}(i + \frac{1}{2}, j + \frac{1}{2}, k) - H_z^{n+1/2}(i - \frac{1}{2}, j + \frac{1}{2}, k)}{\Delta x} \\ & = \epsilon(i, j + \frac{1}{2}, k) \frac{E_y^{n+1}(i, j + \frac{1}{2}, k) - E_y^n(i, j + \frac{1}{2}, k)}{\Delta t} \\ & + \frac{\sigma(i, j + \frac{1}{2}, k)}{2} (E_y^{n+1}(i, j + \frac{1}{2}, k) + E_y^n(i, j + \frac{1}{2}, k)) \\ & + J_{y,src}(i, j + \frac{1}{2}, k), \quad (25) \end{aligned}$$

and

$$\begin{aligned} & \frac{E_x^n(i + \frac{1}{2}, j, k + 1) - E_x^n(i + \frac{1}{2}, j, k)}{\Delta z} \\ & - \frac{E_z^n(i + 1, j, k + \frac{1}{2}) - E_z^n(i, j, k + \frac{1}{2})}{\Delta x} \\ & = -\mu(i + \frac{1}{2}, j, k + \frac{1}{2}) \\ & \frac{H_y^{n+1/2}(i + \frac{1}{2}, j, k + \frac{1}{2}) - H_y^{n-1/2}(i + \frac{1}{2}, j, k + \frac{1}{2})}{\Delta t}. \quad (26) \end{aligned}$$

These can be trivially manipulated to solve for a time updated E_y and H_y in the form of

$$\begin{aligned} & E_y^{n+1}(i, j + \frac{1}{2}, k) \\ & = a(i, j + \frac{1}{2}, k) \left\{ b(i, j + \frac{1}{2}, k) E_y^n(i, j + \frac{1}{2}, k) \right. \\ & + \frac{1}{\Delta z} \left[H_x^{n+1/2}(i, j + \frac{1}{2}, k + \frac{1}{2}) - H_x^{n+1/2}(i, j + \frac{1}{2}, k - \frac{1}{2}) \right] \\ & - \frac{1}{\Delta x} \left[H_z^{n+1/2}(i + \frac{1}{2}, j + \frac{1}{2}, k) - H_z^{n+1/2}(i - \frac{1}{2}, j + \frac{1}{2}, k) \right] \\ & \left. - J_{y,src}(i, j + \frac{1}{2}, k) \right\}, \quad (27) \end{aligned}$$

and

$$\begin{aligned} & H_y^{n+1/2}(i + \frac{1}{2}, j, k + \frac{1}{2}) = H_y^{n-1/2}(i + \frac{1}{2}, j, k + \frac{1}{2}) \\ & - \frac{\Delta t}{\mu(i + \frac{1}{2}, j, k + \frac{1}{2}) \Delta z} \left[E_x^n(i + \frac{1}{2}, j, k + 1) - E_x^n(i + \frac{1}{2}, j, k) \right] \\ & + \frac{\Delta t}{\mu(i + \frac{1}{2}, j, k + \frac{1}{2}) \Delta x} \left[E_z^n(i + 1, j, k + \frac{1}{2}) - E_z^n(i, j, k + \frac{1}{2}) \right], \quad (28) \end{aligned}$$

where a and b are update coefficients defined by

$$a(i, j, k) = \left[\frac{\epsilon(i, j, k)}{\Delta t} + \frac{\sigma(i, j, k)}{2} \right]^{-1}, \quad (29)$$

and

$$b(i, j, k) = \left[\frac{\epsilon(i, j, k)}{\Delta t} - \frac{\sigma(i, j, k)}{2} \right]. \quad (30)$$

Similarly, the remaining update equations for E_x, E_z, H_x and H_z are

$$\begin{aligned} & E_x^{n+1}(i + \frac{1}{2}, j, k) \\ & = a(i + \frac{1}{2}, j, k) \left\{ b(i + \frac{1}{2}, j, k) E_x^n(i + \frac{1}{2}, j, k) \right. \\ & + \frac{1}{\Delta y} \left[H_z^{n+1/2}(i + \frac{1}{2}, j + \frac{1}{2}, k) - H_z^{n+1/2}(i + \frac{1}{2}, j - \frac{1}{2}, k) \right] \\ & - \frac{1}{\Delta z} \left[H_y^{n+1/2}(i + \frac{1}{2}, j, k + \frac{1}{2}) - H_y^{n+1/2}(i + \frac{1}{2}, j, k - \frac{1}{2}) \right] \\ & \left. - J_{x,src}(i + \frac{1}{2}, j, k) \right\}, \quad (31) \end{aligned}$$

$$\begin{aligned} & E_z^{n+1}(i, j, k + \frac{1}{2}) \\ & = a(i, j, k + \frac{1}{2}) \left\{ b(i, j, k + \frac{1}{2}) E_z^n(i, j, k + \frac{1}{2}) \right. \\ & + \frac{1}{\Delta x} \left[H_y^{n+1/2}(i + \frac{1}{2}, j, k + \frac{1}{2}) - H_y^{n+1/2}(i - \frac{1}{2}, j, k + \frac{1}{2}) \right] \\ & - \frac{1}{\Delta y} \left[H_x^{n+1/2}(i, j + \frac{1}{2}, k + \frac{1}{2}) - H_x^{n+1/2}(i, j - \frac{1}{2}, k + \frac{1}{2}) \right] \\ & \left. - J_{z,src}(i, j, k + \frac{1}{2}) \right\}, \quad (32) \end{aligned}$$

$$\begin{aligned} & H_x^{n+1/2}(i, j + \frac{1}{2}, k + \frac{1}{2}) = H_x^{n-1/2}(i, j + \frac{1}{2}, k + \frac{1}{2}) \\ & - \frac{\Delta t}{\mu(i, j + \frac{1}{2}, k + \frac{1}{2}) \Delta y} \left[E_z^n(i, j + 1, k + \frac{1}{2}) - E_z^n(i, j, k + \frac{1}{2}) \right] \\ & + \frac{\Delta t}{\mu(i, j + \frac{1}{2}, k + \frac{1}{2}) \Delta z} \left[E_y^n(i, j + \frac{1}{2}, k + 1) - E_y^n(i, j + \frac{1}{2}, k) \right], \quad (33) \end{aligned}$$

and

$$\begin{aligned}
H_z^{n+1/2}(i + \frac{1}{2}, j + \frac{1}{2}, k) &= H_z^{n-1/2}(i + \frac{1}{2}, j + \frac{1}{2}, k) \\
&- \frac{\Delta t}{\mu(i + \frac{1}{2}, j + \frac{1}{2}, k)\Delta x} \left[E_y^n(i + 1, j + \frac{1}{2}, k) - E_y^n(i, j + \frac{1}{2}, k) \right] \\
&+ \frac{\Delta t}{\mu(i + \frac{1}{2}, j + \frac{1}{2}, k)\Delta y} \left[E_x^n(i + \frac{1}{2}, j + 1, k) - E_x^n(i + \frac{1}{2}, j, k) \right].
\end{aligned} \quad (34)$$

The Dirichlet PEC boundary condition found in (9) is integrated in (27) and (31-32) via defining E_x, E_y and E_z on the $i = 0, j = 0$ and $k = 0$ planes to be inside of the PEC region in the case of the rectangular cavity resonator. Thus after these fields are initialized to zero, they are never updated. For verification purposes the PEC condition on the $k = 0$ plane will be replaced by Mur's ABC as to give the appearance of an infinite waveguide to a propagating wave.

The same Dirichlet boundary condition can be enforced in (28) and (33-34) by setting any electric fields outside the boundary region to zero on the $i = i_{\max}, j = j_{\max}$, and $k = k_{\max}$ planes.

In the case of the infinite waveguide, the PEC condition at the $k = k_{\max}$ plane may cause fictitious reflections from waves with frequencies below the cutoff frequency f_c of the TE₁₀ mode. These reflections are assumed to be negligible for the purposes of this analysis.

2) *TF/SF 1-way Source*: Using the linear nature of Maxwell's Equations, E_y and H_x fields can be injected into the simulation by 'correcting' the curl equations at an arbitrary source plane $k = k_{src}$ on the primordial grid. As shown in Fig. 1, the TF/SF source exists near $k = k_{\max}$, thus we define $k \in [0, k_{src}]$ to be the total-field region and $k \in (k_{src}, k_{\max}]$ to be the scattered-field region. The distinction between regions allows for the study of reflected field profiles for fields below the cutoff frequency.

Corrections for the inclusion of an H_x source field in E_y manifest as

$$\begin{aligned}
E_y^{n+1}(i, j + \frac{1}{2}, k_{src}) &= E_y^{n+1}(i, j + \frac{1}{2}, k_{src}) \\
&- \frac{\Delta t}{\epsilon(i, j + \frac{1}{2}, k_{src})\Delta z} H_{x,src}(i, j + \frac{1}{2}, k_{src} + \frac{1}{2}),
\end{aligned} \quad (35)$$

and

$$\begin{aligned}
E_y^{n+1}(i, j + \frac{1}{2}, k_{src} - 1) &= E_y^{n+1}(i, j + \frac{1}{2}, k_{src} - 1) \\
&+ \frac{\Delta t}{\epsilon(i, j + \frac{1}{2}, k_{src})\Delta z} H_{x,src}(i, j + \frac{1}{2}, k_{src} - 1 + \frac{1}{2}).
\end{aligned} \quad (36)$$

Similarly, corrections for the inclusion of an E_y source field in H_z are expressed as

$$\begin{aligned}
H_x^{n+1/2}(i, j + \frac{1}{2}, k_{src} + \frac{1}{2}) &= H_x^{n+1/2}(i, j + \frac{1}{2}, k_{src} + \frac{1}{2}) \\
&- \frac{\Delta t}{\mu(i, j + \frac{1}{2}, k_{src} + \frac{1}{2})\Delta z} E_{y,src}^n(i, j, k_{src}),
\end{aligned} \quad (37)$$

and

$$\begin{aligned}
H_x^{n+1/2}(i, j + \frac{1}{2}, k_{src} - \frac{1}{2}) &= H_x^{n+1/2}(i, j + \frac{1}{2}, k_{src} - \frac{1}{2}) \\
&+ \frac{\Delta t}{\mu(i, j + \frac{1}{2}, k_{src} - \frac{1}{2})\Delta z} E_{y,src}^n(i, j, k_{src}).
\end{aligned} \quad (38)$$

When combined with source fields defined in (13)-(14) these equations allow energy to be injected into the system in the form of a 1-way source wave propagating in a rectangular waveguide [4].

3) *Mur Absorbing Boundary Condition*: In order to reformulate the Engquist-Majda ABC of (18) into Mur's absorbing boundary condition, the split derivative term must be approximated as

$$\begin{aligned}
\frac{\partial^2 U^n(i, j, \frac{1}{2})}{\partial z \partial t} &\approx \frac{1}{2\Delta t} \left[\frac{U^{n+1}(i, j, 1) - U^{n+1}(i, j, 0)}{\Delta x} \right. \\
&\quad \left. - \frac{U^{n-1}(i, j, 1) - U^{n-1}(i, j, 0)}{\Delta x} \right]
\end{aligned} \quad (39)$$

as in [4].

The remaining derivatives are able to be approximated by (23-24). With these approximate derivatives, the most time advanced field component is updated with

$$\begin{aligned}
U^{n+1}(i, j, 0) &= -U^{n-1}(i, j, 1) \\
&+ \frac{c\Delta t - \Delta z}{c\Delta t + \Delta z} \left[U^{n+1}(i, j, 1) - U^{n-1}(i, j, 0) \right] \\
&+ \frac{2\Delta z}{c\Delta t + \Delta z} \left[U^n(i, j, 0) + U^n(i, j, 1) \right] \\
&+ \frac{(c\Delta t)^2 \Delta z}{2\Delta x^2 (c\Delta t + \Delta z)} \left[U^n(i + 1, j, 0) - 2U^n(i, j, 0) \right. \\
&\quad \left. + U^n(i - 1, j, 0) + U^n(i + 1, j, 1) \right. \\
&\quad \left. - 2U^n(i, j, 1) + U^n(i - 1, j, 1) \right] \\
&+ \frac{(c\Delta t)^2 \Delta z}{2\Delta y^2 (c\Delta t + \Delta z)} \left[U^n(i, j + 1, 0) - 2U^n(i, j, 0) \right. \\
&\quad \left. + U^n(i, j - 1, 0) + U^n(i, j + 1, 1) \right. \\
&\quad \left. - 2U^n(i, j, 1) + U^n(i, j - 1, 1) \right]
\end{aligned} \quad (40)$$

which is the 3D variant of Mur's absorbing boundary condition for $k = 0$ [4]. This condition will only be used for validating the waveguide and will be removed for the analysis of cavity resonators.

III. NUMERICAL RESULTS

All update equations as defined in Section II-C were implemented in Rust. This language was chosen for its C++ like performance while enforcing compile-time memory safety which makes writing fast and safe CEM codes relatively easy. An overview of this implementation can be found in V-A.

A. Verification and Validation

To verify and validate model results, the case of an infinitely long waveguide with fields propagating in the TE₁₀ mode.

This case is chosen as simulated results can easily be compared to analytic results.

All verification and validation analyses are performed with 0.1m stretch of a WR-90, X-band waveguide with a free space-filled, cross section of $a = 0.02286\text{m}$ and $b = 0.01016\text{m}$ [9]. Said configuration has an analytic TE_{10} cutoff frequency of as calculated by

$$f_c = \frac{c}{2\pi\sqrt{\epsilon_r\mu_r}}\sqrt{\left[\frac{m\pi}{a}\right]^2} \quad (41)$$

from [1]. Using free space dielectric parameters, this geometry has a cutoff frequency of 6.557GHz for the TE_{10} mode.

To ensure waves above the cutoff frequency are able to freely propagate, a monochromatic source as defined by (15) is used with a 10GHz carrier frequency with a ramp time of 5ns is used as an E_y driver function. The simulation was carried out using a time step of $\Delta t = 1.863\text{ps}$ over a 25ns duration with spatial steps as $\Delta x = 0.994\text{mm}$, $\Delta y = 0.923\text{mm}$, and $\Delta z = 0.990\text{mm}$.

A spatial field profile of this system can be found in Fig. 2 along the y and x centerline planes.

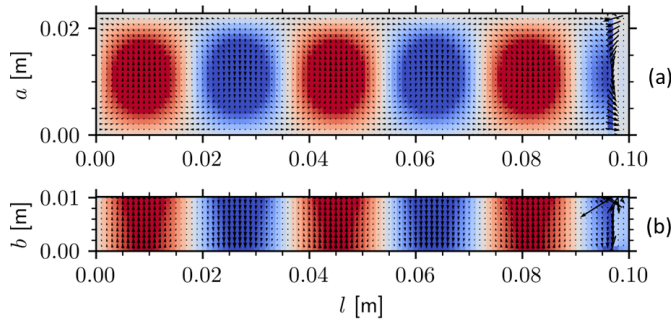


Fig. 2: Source Profiles at $t = 8.191\text{ns}$ for (a) E_y intensity (colored) with H_x, H_y directions (arrows) along the $y = 5.538\text{mm}$ plane and (b) H_x intensity (colored) with E_y, E_z directions (arrows) along the $x = 11.926\text{mm}$ plane

Arrows in Fig. 2 were scaled as to best show direction where as intensity colors were based off of the E_y sinusoidal amplitude. Colors for Fig. 2 (b) are scaled down by E_y/η_{10} as in (12). Field intensity was not explicitly labeled in Fig. 2 as it cluttered the plots and is not relevant for this analysis.

From visual inspection, it is quite clear that these field profiles match the theoretical frequency domain profiles as given in (11-12). Additionally, the validity of the TF/SF source and Mur's ABC is apparent from the relatively small fields found in the upper right of Fig. 2 (a) and (b). The small discrepancy in the upper right corner of 2 (b) is explained by leakage of the TF/SF source interacting with the PEC corner; both of which are liable for discrepancies as mentioned in [2].

To ensure the integrity of the wave propagating along the length of the waveguide, frequency spectra are taken of the source total field and transmitted total E_y field as found in Fig. 3. These transmitted and source spectra were taken at two representative voxels at $z = 4.950\text{mm}$ and $z = 95.050\text{mm}$ along the same x and y centerlines of Fig. 2. This choice of a centerline is arbitrary; changes in the x position would

decrease the relative field intensity due to the sinusoidal profile necessitated by the PEC walls. Data for this plot was obtained by taking a field 'snapshot' 2,000 times over a the span of the 25ns simulation window with intermediate time spacing between samples of 13.043ps.

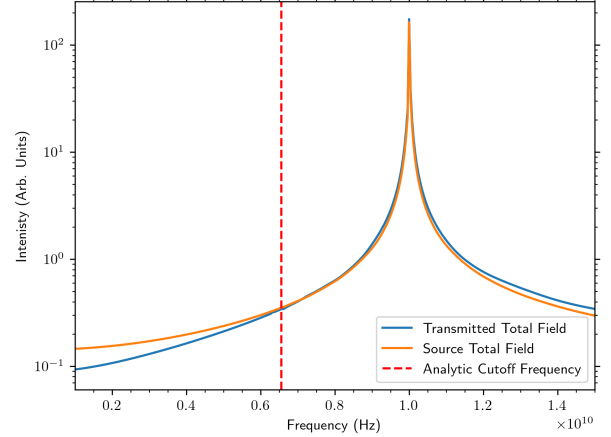


Fig. 3: Transmitted and Source Frequency Spectra with Labeled Cutoff Frequency for 10GHz Monochromatic Tapered Sine E_y Source

Fig. 3 clearly shows that all frequencies above the 6.557GHz cutoff frequency are able to travel along the length of the waveguide with minimal loss. These signals only differ for frequencies below that of the cutoff frequency of which fields are not able to propagate indefinitely.

With frequencies above the cutoff frequency able to freely propagate in the waveguide, it is now important to assess the waveguides performance in attenuating waves below the cutoff frequency. To test this property of our simulated waveguide, a wide-band modulated gaussian pulse as in (16) is used as a driver signal with a carrier frequency of 10GHz, ramp time of 0.5ns and delay time of 3ns. Frequency spectra at identical locations to that of Fig. 3 can be found below in Fig. 4. To facilitate the additional frequency content of the modulated Gaussian, field snapshots were taken at all 13,417 time steps over the simulation's 25ns duration.

As shown above in Figure 4 the *in silico* waveguide exhibits a cutoff frequency of approximately 6.2GHz which only differs from the theoretical by 5.444% making this model relatively realistic. Below this cutoff frequency, Fig. 4 shows a nearly two order of magnitude reduction in the transmitted while having little overall impact on frequencies above this which is expected.

B. Analysis of Unloaded Quality Factor with Varying Dielectric Loss

With the waveguide now successfully validated, the resonator performance can now be assessed using different dielectric materials. More specifically, we aim to compare the performance of a cavity resonator filled with beeswax to that filled with beryllia at a frequency of 10GHz. Material

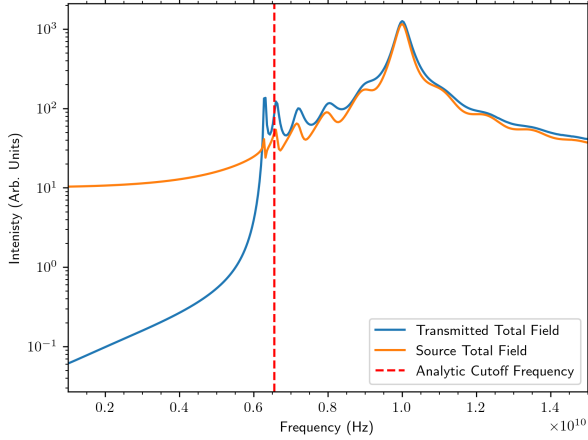


Fig. 4: Transmitted and Source Frequency Spectra with Labeled Cutoff Frequency for 10GHz Center Frequency, 0.5ns Ramp Time, Modulated Gaussian Pulse

properties for these materials are obtained from [1] which are used to derive conductivities for these materials at 25°C . For simplicity, the resonator cavity length is reduced from 0.1m to 0.05m to reduce the computational domain. An identical wideband carrier signal to that found in Fig 4 is used to look for resonances in these materials at and around 10GHz. For these simulations, the centermost E_y voxel is used as a representative sample of the whole domain. Due to these materials differing relative permittivities, the centermost voxel may exist at slightly different physical locations within the simulation; however, this discrepancy is assumed to be small. results for this comparative study can be found below in Fig. 5.

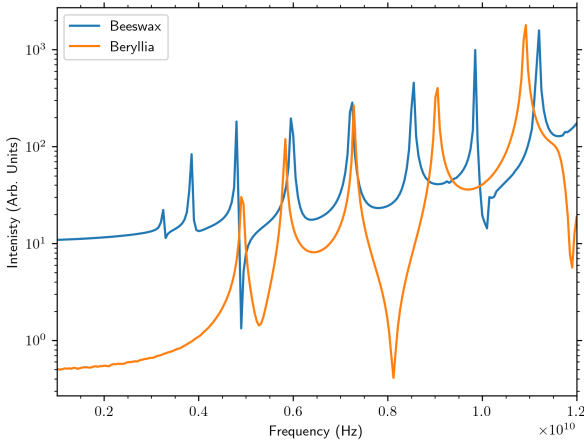


Fig. 5: Centermost Voxel Frequency Spectra for Beeswax and Beryllia for 10GHz Center Frequency, 0.5ns Ramp Time, Modulated Gaussian Pulse

These two materials exhibit far more complex interactions than that of free space with numerous resonances excited in

both materials. With its lower loss tangent of $\tan \delta = 0.0003$ and higher unloaded dielectric quality factor $Q = 3333.3$, beryllia resonates several times more than beeswax with a loss tangent of $\tan \delta = 0.005$ and $Q = 200$ at 10GHz. Interestingly the beeswax-filled cavity resonator exhibits more peaks than that of beryllia over the 1 – 12GHz domain. This is likely a direct result of the complex interaction between resonator shape, dielectric properties, and wavelength as described in [1].

IV. CONCLUSION

A 3-dimensional finite difference time domain was developed from Maxwell's Equations for a rectangular waveguide and cavity resonator. The model was validated against analytic results for narrow and wide band signals thereby verifying the model's calculated fields. From this, several dielectric materials were compared for use in X-Band cavity resonators at 10GHz. These compared results were then explained using theoretical unloaded quality factors further verifying the accuracy of the model.

While relatively performant, there are many optimizations that could be made to the underlying implementation. Most notably tiled approaches could be taken to improve program cache locality to alleviate the memory bound nature of the loops in this implementation. Tiled approaches would also aid in exploiting the embarrassingly parallel structure Yee's FDTD algorithm gives rise to. Further improvements could also be made to the implementation to allowing for more complex geometries to be represented which may be useful for placing devices inside waveguides or using the waveguide as a source for another device. Finally, the user experience of this implementation should be improved as it is remarkably easy to save in tens to hundreds of gigabytes of data inadvertently shifting the bottleneck away from memory to disk performance.

V. APPENDIX

A. Code Structure

Code is broken up into logical modules, as is custom in Rust, which contain related aspects of the code. The file `./src/main.rs` contains the 'main' function that is built into a binary. The file `./src/solver.rs` contains a high level interface for interacting with and bootstrapping the simulation. The file `./src/geometry.rs` contains a structure that holds information relevant to the geometry of the simulation. Finally, the `./src/engine.rs` contains all data and methods needed to evolve the simulation in time and contains much of the simulation code. All functions are commented using function comments in the source code which are automatically assembled into an interactive webpage containing all project documentation. Said documentation can be found under the `./doc/` directory. As such project documentation can either be viewed by looking at the source code and/or viewing the interactive documentation pages by opening `./doc/waveguide/index.html` with a web browser. The code can easily be compiled with cargo (the package manager that comes with Rust much like Pip for Python) using the command `cargo build --release`.

The compiled binary can then be executed by running `./target/release/driver.exe`. This binary reads in data from `config.toml` which contains all simulation parameters.

REFERENCES

- [1] D. M. Pozar, *Microwave Engineering*. John Wiley & Sons, 2011.
- [2] T. E. Roth, *ECE 61800 Lecture Notes*. Purdue University, 2024.
- [3] K. S. Yee, "Numerical solution of initial boundary value problems involving maxwell's equations in isotropic media," *IEEE Transactions on Antennas and Propagation*, vol. 14, no. 3, 1966.
- [4] S. C. H. Allen Taflov, *Computational Electrodynamics The Finite-Difference Time-Domain Method*. Artec House Inc., 2005.
- [5] T. V. D. Simon Ramo, John R. Whinnery, *Fields and Waves in Communication Electronics*. John Wiley and Sons, 1994.
- [6] J. B. Schneider, "Understanding the finite-difference time-domain method," www.eecs.wsu.edu/~schneidj/ufdtd, 2010, [Online; accessed 28-February-2024].
- [7] R. C. Rumpf, "Implementation of one-dimensional fdttd," <https://empossible.net/wp-content/uploads/2020/01Lecture-Implementation-of-1D-FDTD.pdf>, 2020, [Online; accessed 28-February-2024].
- [8] J.-M. Jin, *Theory and Computation of Electromagnetic Fields*. John Wiley & Sons, 2011.
- [9] Everything RF contributors, "Rectangular waveguide sizes," <https://www.everythingrf.com/tech-resources/waveguides-sizes>, 2021, [Online; accessed 28-February-2024].